



Virtual quality assessment tools for material extrusion processes

R. Jill Urbanic ^a, Chris G. Burford ^b and Robert W. Hedrick ^b

^aUniversity of Windsor, Canada; ^bCAMufacturing Solutions Inc, Canada

ABSTRACT

Additive Manufacturing (AM) material extrusion systems are being developed to expand into new markets. Although complex components can be readily fabricated with this process family, voids are inherently generated as well as several travel path segments per layer. Simulation models that generate information with respect to the travel paths and void locations would provide a baseline for process planning comparisons. Consequently, developing virtual quality assessment tools is the focus of this research. ‘Macro’ and ‘micro’ information is generated for each tool path – layer set, and plotted using Excel[®] and R tools, as illustrated by several case studies. This information can be utilized for statistical evaluations and downstream optimization.

KEYWORDS

Material extrusion; virtual void locations; tool path; statistics

1. Introduction

The material extrusion additive manufacturing (AM) process family includes the well-established fused deposition modeling (FDM) process [16], and processes presently under development such as the ‘Big Area Additive Manufacturing’ (BAAM) [4], large scale additive manufacturing, (LSAM) [11], and Medium Area Additive Manufacturing (MAAM) [12] processes. Layers are built from molten thermoplastic filaments or fibre-reinforced filaments. The general material extrusion process characteristics are similar, as material is fed through a temperature-controlled head and extruded when it is in a semi-viscous state. However, the bead size and shape vary for these processes, as the beads may vary from 0.25 mm in width (fused deposition modelling process) to 12 mm (large scale additive manufacturing). The beads may be ellipsoid or obround in shape, and ‘side to side’ and interlayer bonding occurs at the bead boundaries. Some processes apply a force onto the extruded bead to facilitate the inter-layer bonding and provide a constant layer height.

The anisotropic properties associated with the layered manufacturing process are well known [2, 9, 14]; however, when exploring mechanical properties for tensile and compressive samples (Fig. 1(a) and (b)) with ‘lightweighting’ internal lattices or voids, unexpected failure results occurred [17] (Fig. 1(c)). The original research goal was to reduce material costs without compromising the product performance characteristics, while

considering the known anisotropic properties between layers. Using a ‘design of experiments’ approach, multiple materials, machines, parametric lattices (cubic, hexagonal, and tetrahedral) and spherical void lattice patterns (based on atomic crystal structures such as primitive, body centred cubic and face centred cubic) were tested. The failure points did not initiate where expected and inconsistent results were observed when evaluating material volume versus tensile and compressive strength relationships. For example, for a compressive specimen built with 3.2 cubic inches of build material, the maximum compressive forces before failure could vary between 19kN to 30 kN. It must be noted that the results for a specific ‘lightweighted’ configuration were repeatable (+/- 1%).

The testing results across a broad range of experiments indicated that material usage could not be correlated to tensile and compressive mechanical strength properties with confidence. It was found that unexpected voids and discontinuities were embedded in the interior (Fig. 1(a)) of the specimens, and these voids and discontinuities are due to the tool path deposition strategy. Although the build volume of material may be close to the CAD model volume, this was no indicator with respect to the ‘quality’ of the interior fill. With large, thick walled components fabricated with a thin slice height (0.13 mm) and small bead width (0.25 mm), the probability of voids existing and creating a performance issue is reduced. However, one of the benefits of AM is the ability to

CONTACT R. Jill Urbanic  jurbanic@uwindsor.ca; Chris G. Burford  chris.burford@camufacturing.com;
Robert W. Hedrick  bob.hedrick@camufacturing.com

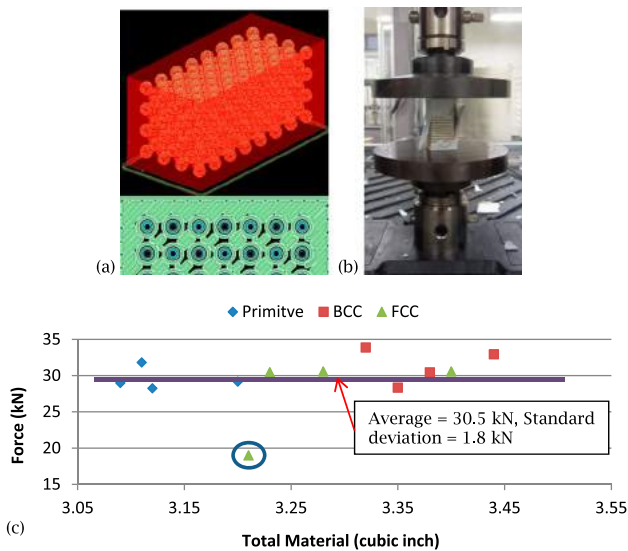


Figure 1. (a) compressive model for samples with primitive, body centred cubic and face centred cubic void patterns with a tool path (Insight[®] software representation) for a face centred cubic specimen, (b) experimental testing, (c) compressive testing results showing the variations in material usage and approximately constant force loading, and different force loading (circle) with similar material usage.

produce complex thin walled components without tooling. Standard strength and vibration control optimization solutions include applying ‘thin wall’ gussets and ribs strategically to provide strength or damping characteristics where required on a product. In these scenarios, voids and discontinuities are problematic. The tool paths/voids for two layers are shown for a casting pattern (pink) gusset (Fig. 2(a)), and an insulator / cable tray (Fig. 2(b)).

These are the ‘best’ case results when exploring the component orientation and standard bead geometry options using commercial software. There are no void

and discontinuity quality checks available in this software, and reviewing each layer manually is time intensive for large parts. For the newer processes that have larger beads (Fig. 3), the problems related to voids and discontinuities are amplified. Consequently, tool path quality assessment tools, which provide insights into void characteristics and discontinuities, need to be developed which complement the material extrusion tool path generation and visualization tools. *The goal of this research is to develop virtual quality assessment data and tools to assist designers with evaluating process planning solution strategies.*

2. Research methodology

Porosity and void analysis tools have been developed for many diverse domains, which include the casting, permeable membrane, and geology domains. Existing technologies focus on both destructive (i.e. cutting a casting into segments) and nondestructive methods (i.e. x-ray) to visual porosity and void patterns to determine the characteristics of the test specimen being evaluated. However, in the additive manufacturing domain, limited research has been performed in this topic area. Research to date has focused on developing products with porous structures, such as tissue scaffolding [6], or investigating selective laser sintering / melting porosity [1- 3, 5, 7, 8, 13]. However, no published research for the AM material extrusion processes is readily available. As the voids for a thermoplastic based material extrusion process are generated by the tool paths, the toolpath characteristics need to be evaluated. Three dimensional tool path visualization strategies / stock models for machining have been developed [10] – these need to be expanded upon to incorporate information related to the travel path fill.

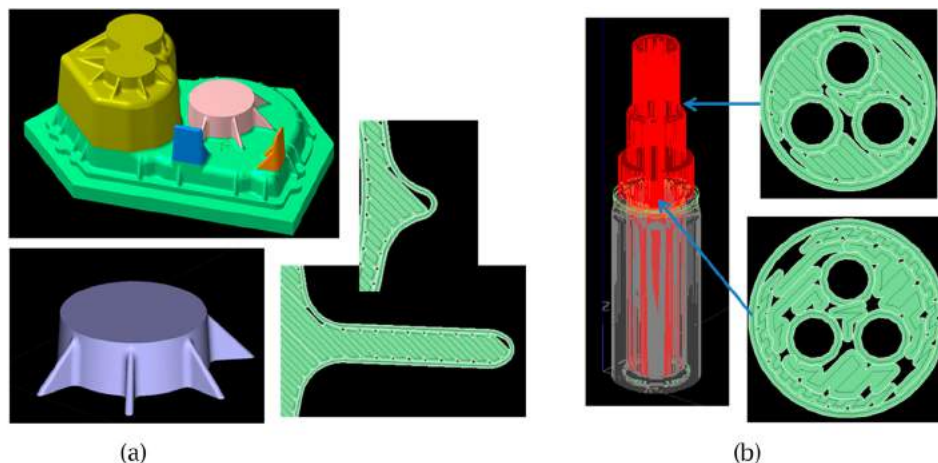


Figure 2. (a) Casting pattern segment, and fill patterns, (b) insulator and fill patterns.

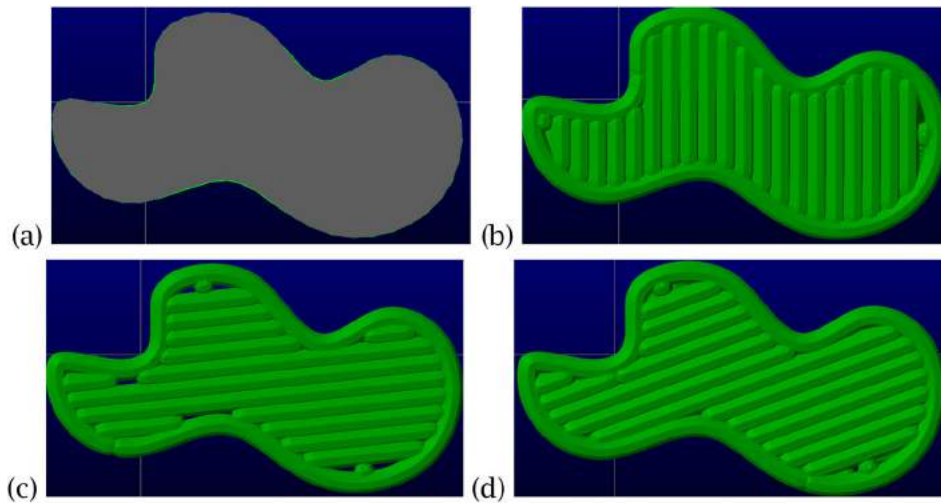


Figure 3. (a) a curvilinear shape with a 6.35 mm bead width (0.25 in) raster angles at (b) 90°, (c) 7° and (d) 20, clearly showing the impact of the raster fill angle on the voids and discontinuities.

With the material extrusion based processes, there is limited overlapping which is possible between the fill layers to each other, and the fill to the boundary layers while maintaining a constant Z height. Consequently, voids and discontinuities result. However, if these conditions can be identified on a macro and micro scale, a process planning solution can be developed to minimize these conditions. To perform a process plan solution evaluation, information with respect to the tool path strategy and the resultant voids needs to be collected and the results displayed. The ‘macro’ data collected is the total travel path length, the void area, and enumerating the tool path segments per layer, while the ‘micro’ data is the x , y , z coordinate of each void, each void’s area, and major axis of each void. This information can be used to evaluate a process planning configuration.

The standard bead deposition fill strategy for each layer consists of boundary contouring and zig-zag tool paths. The input parameters for this research are:

- Boundary and fill bead width & height
- Number of boundary beads
- Boundary pass overlap (for multiple contours) as a % of the bead width
- Maximum pass overlap as a % of the bead width
- Stop / start overlap as a % of the bead width
- Fill type (zig-zag or one way)
- Fill pass overlap (for multiple contours) as a % of the bead width
- Maximum pass overlap as a % of the bead width
- Boundary to fill overlap as a % of the bead width
- Starting fill angle
- Change in angle per layer

The operation order, 5 axis motion, contour offsets and other related process parameters are not considered, as they are related to the motion control. The travel path related to rapid motion is not included in the analysis.

There are 6 case studies considered for this research: all are simple extrusions. The shapes employed for this work are a set of n -gons (4, 7, 11 sides), a plate with holes which is compared to the Insight[®] solution visually, and two complex shapes: a timing mechanism, and a Celtic knot (Fig. 4). The standard bead width is 1 mm. The bead width is constant for the tool path testing unless otherwise noted, and the allowable boundary pass overlap range is 15–50%. The stop/start overlap is set to 50%. One, two, and three contour beads (with fill) and 100% boundary fill options are explored as noted. The fill overlap range is 10–15%, and boundary to fill overlap is 25%. The starting raster angle is 0°, and the increment angle is 1°. The slice height is segmented into 91 layers to create a solution for all raster increments between 0–90°. This allows for direct geometry- raster fill angle – fill comparisons. A sample set of solutions for the 5 hole block and the 11-sided polygon is presented in Fig. 5.

The total travel path length (this included the motions only when the material is deposited; there are no rapid moves included in this value), the total void area for a layer, and the number of tool path segments are calculated for each raster angle-layer set. This ‘macro’ data is output into a CSV file. It is assumed that more material is deposited with longer the tool path lengths per layer. The discontinuities introduce potential failure points; consequently, the number of travel path segments per layer directly reflects the number of discontinuities. The total void area is determined separately, as there are allowable

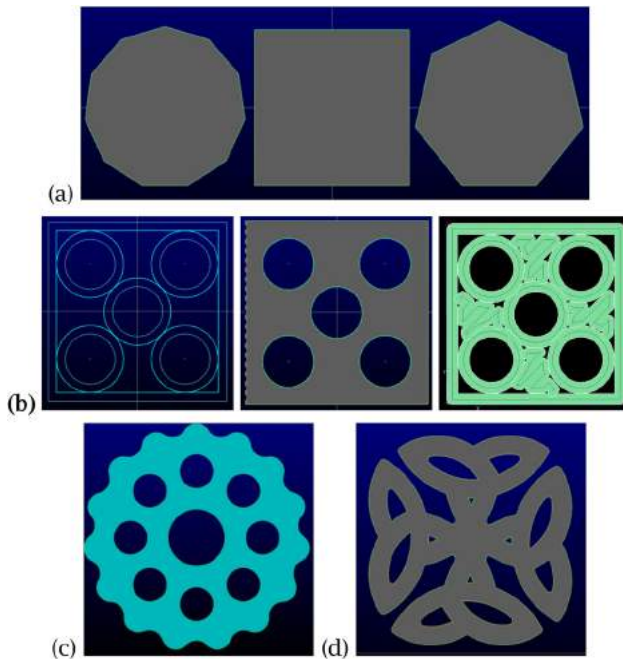


Figure 4. (a) 11-sided polygon, square, heptagon (b) a plate with five holes, showing the width of a boundary bead, the solid model, and the Insight[®] tool path, (c) the timing mechanism, and (d) the Celtic knot.

overlap conditions, which will allow for more material to be deposited in a particular region; hence, the travel length is not a complete indicator of the fill volume for a given layer.

A secondary CSV file contains information for each void centroid, the void area, and the major axis length to provide the ability to perform a detailed analysis with respect to the void positions. The voids are plotted using Excel[®] graphing tools and R 3D plotting tools [15] to create void maps.

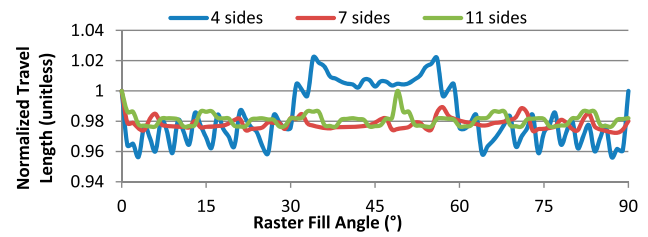


Figure 6. Normalized n-gon tool path strategies for one boundary contour and a raster fill.

The tool path travel length and void data are normalized to the one boundary bead-0° fill raster solutions. These 3D plots and normalized data sets can be employed to determine optimal conditions. A comparison of the normalized tool paths for the n-gons is presented in Fig. 6. It can be seen that the best fill angles are between 34-56° degrees for the square with 34° and 56° being optimal, 57° and 71° degrees for the heptagon, and 0° and 49° for the 11-sided n-gon.

With this data, statistical analyses can be performed to characterize the voids, and the void patterns, and geometric analyses can be performed to determine whether there could be leak paths or chimneys due to voids being present in the same locations on contiguous layers.

Therefore, the AM material extrusion system void visualization strategies are: generate ‘macro’ tool path data and ‘micro’ void data based on the tool path characteristics; plot the voids using Excel[®] and algorithms developed in R; normalize the tool path lengths and macro void data, and with the number of tool path segments, plot the results for comparisons; and perform basic statistical analyses to explore the void size, shape, and frequency characteristics. This is discussed in the next section.

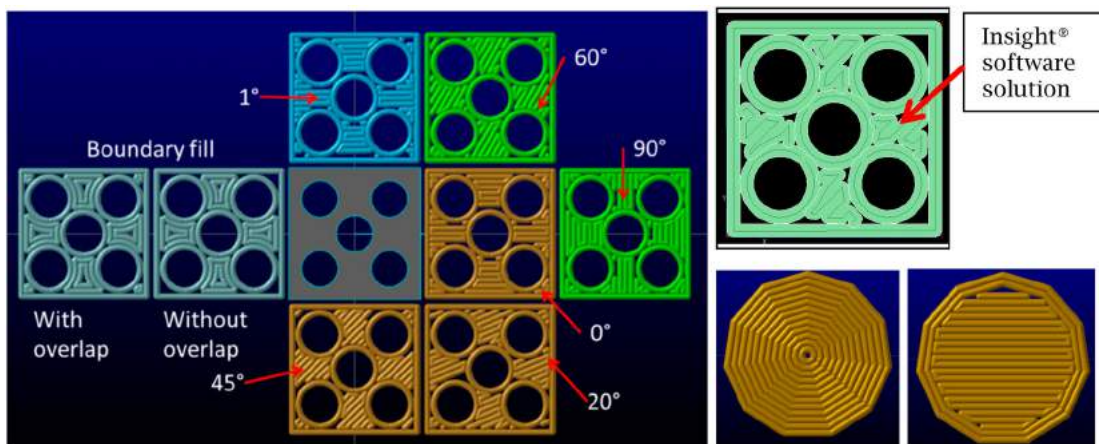


Figure 5. One boundary curve with various raster angle fill strategies & 100% boundary fill for the block with holes, and the 11-sided polygon with 100% boundary fill and a two bead contour-0° raster fill.

3. Results

3.1. N-Gon shapes

For all raster fill angles, the void locations for the polygon shapes are located along the periphery, as shown in Fig. 7(a). There are variations in the number and size of the voids, but the average void size is small (Tab. 1 and Fig. 8). The four sided component has the most voids, and the largest void size, but the smallest average void size. When applying a filter, it can be seen that there are few large voids for this component. The opposite is true for the 11 sided n-gon. For each shape, the information related to the total travel length and number of unique segments (Figure 9) for the associated raster fill angles is presented in Table 2.

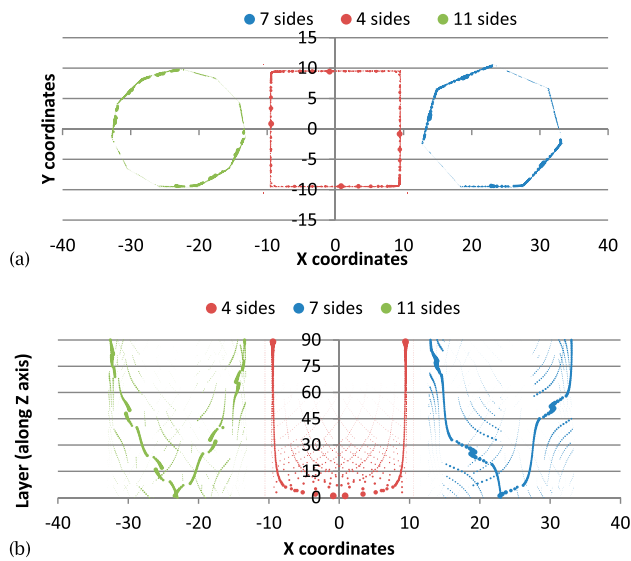


Figure 7. (a) 2D view of the voids, (b) the void positions per layer (layer number is the raster fill angle).

Table 1. Void summary for n-gon shapes.

Shape	No. of Voids	Max. Area (mm) ²	Min. Area (mm) ²	Ave. Area (mm) ²	No. of Voids > 2 mm ²
4 sides	2279	7.59	< 0.004	0.18	20
7 sides	2308	4.97	< 0.004	0.17	30
11 sides	1653	3.16	< 0.004	0.23	41

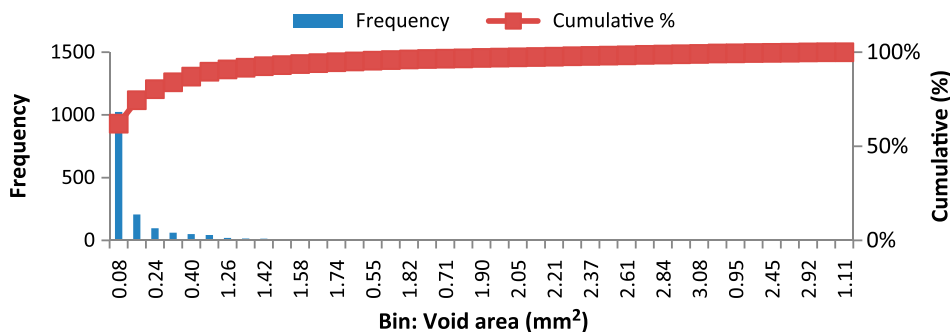


Figure 8. Frequency chart clustering the void areas and frequencies for the 11 sided n-gon.

3.2. 5 Hole plate

For the plate with 5 holes, the influence with the number of boundary contours is explored as well as the raster fill angle. The normalization for this case study is performed with the one boundary bead – 0° raster fill angle as the base line. The configuration that provided the longest travel length consists of one boundary bead. Introducing no or two boundary beads reduces the travel length (Fig. 10(a)). The travel length is consistent amongst all raster fill angles for the two boundary bead configuration. There are noticeable variations for the ‘fill only’ configuration. The subsequent analysis is for the one boundary bead scenario.

The line segments vary between 18 and 31 (Fig. 10(b)). The average number of segments is 20.7 ± 2.5 from 20° – 70°. For the baseline scenario, the voids for a single layer (raster fill angle = 0°), and the voids for all layers are shown in Fig. 10(c) and (d). The void frequency is shown in Fig. 10(e). There are notably less total voids for the 1° raster fill angle, and many voids between 20° - 70°. It can be seen that between the 20° - 70° raster fill angles, there are less discontinuities, but more scattered voids. To understand the void characteristics, a frequency diagram for layers for two distinct build scenarios (1° and 30° raster fill) is generated. This comparison clearly illustrates the void size-frequency conditions. This is illustrated in Fig. 11.

As these material extrusion AM processes are being employed to manufacture functional parts, research needs to be performed to determine which void scenario is preferred with respect to the expected performance characteristics. The crack propagation mechanisms, as well as the damping behavior, will be influenced by the void size, shape, and distribution, but these phenomena are unknown at this time.

3.3. Timing gear

The timing gear has a bounding box 118.85×119.39 mm. Process scenarios are compared with 1 and 2 mm

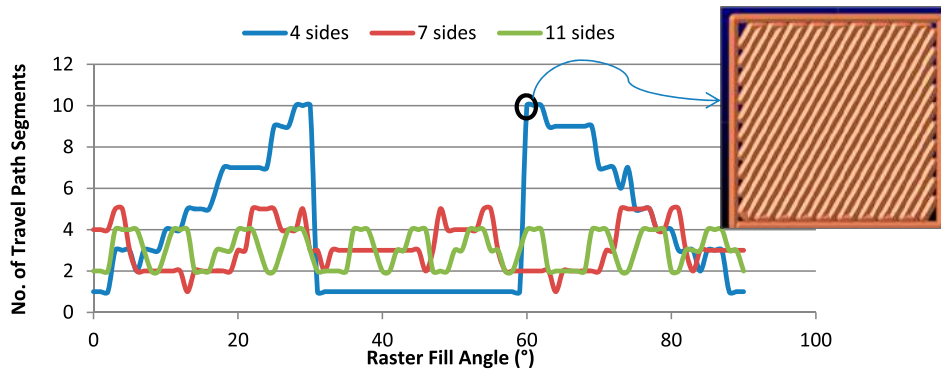


Figure 9. Number of travel path segments for 0–90° raster fill angles, and a blow up for the 60° solution for the 4-sided shape. Note: there is no cornering geometry along the vertical edges due to the allowable geometry overlap constraints.

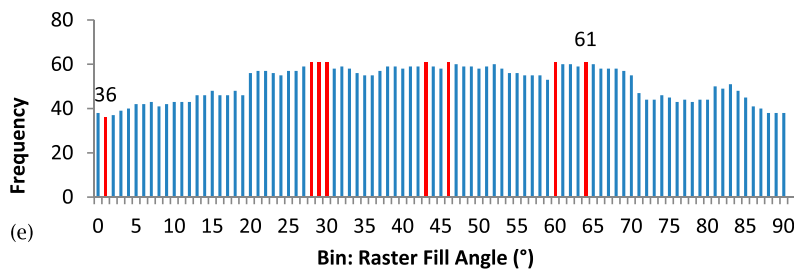
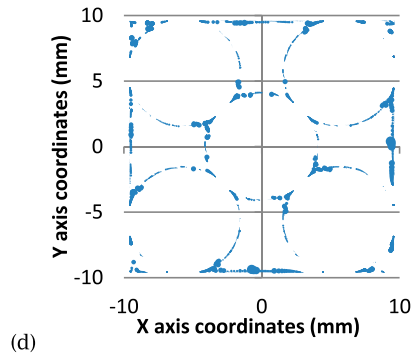
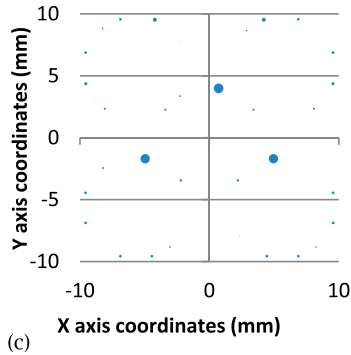
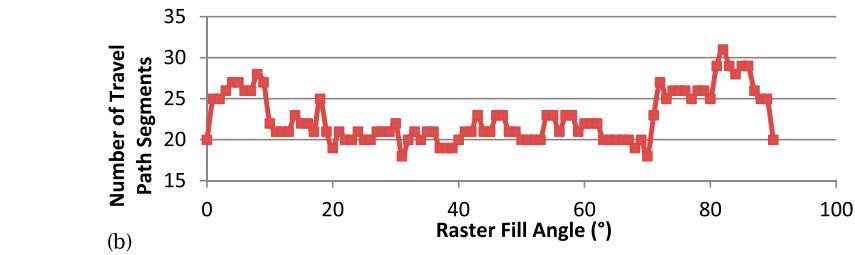
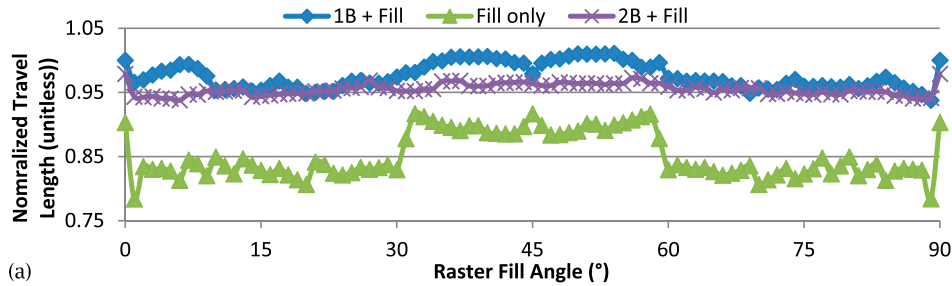


Figure 10. (a) Normalized tool path strategies for selected boundary contours and a raster fill (b) the number of travel path segments, (c) the voids for raster angle = 0, (d) the voids for the complete part, and (e) the void frequency per raster angle, with the voids for the red data presented.

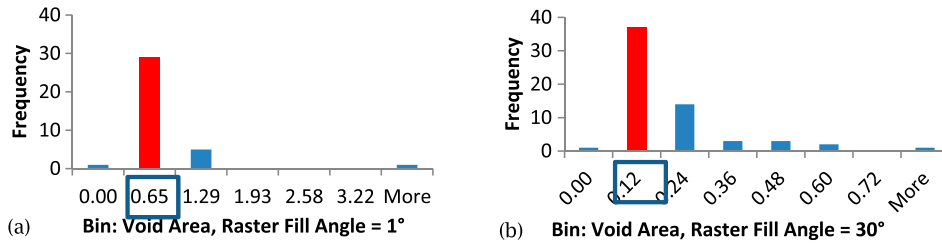


Figure 11. (a) Void area frequencies for the 1° raster fill, and (b) void area frequencies for the 30° raster fill.

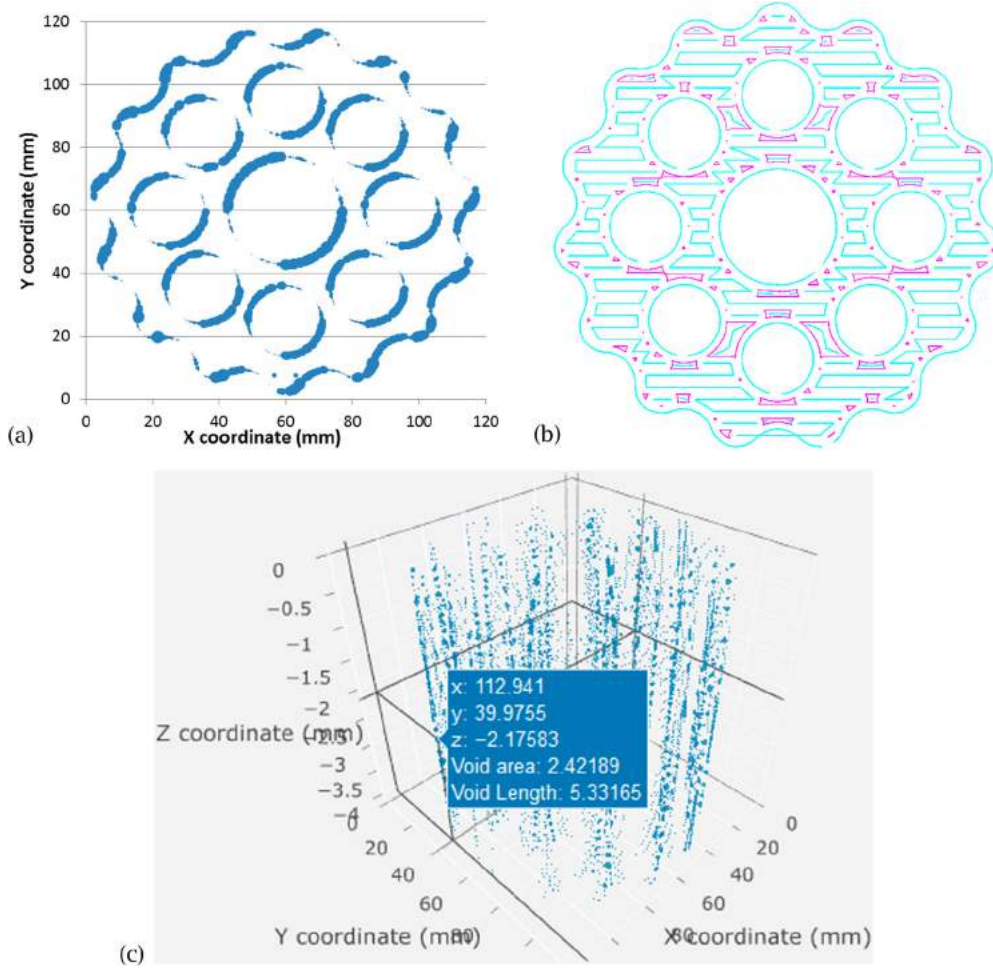


Figure 12. (a) 2D voids, (b) highlighted void regions for a 0° raster fill, and (c) R model (bead width = 1 mm).

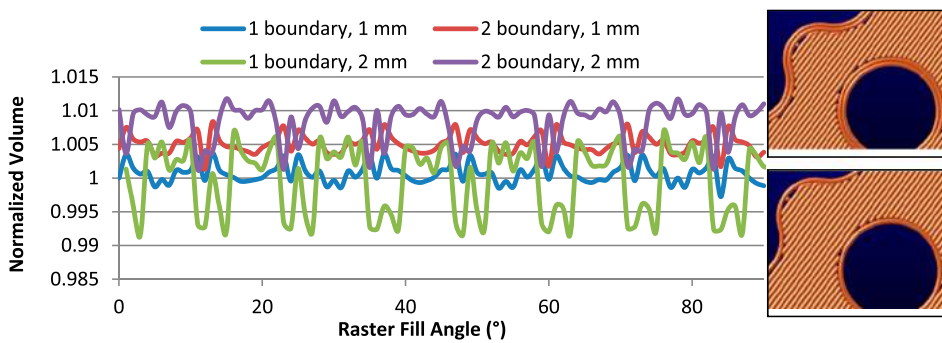


Figure 13. Normalized tool path / volume strategies for selected boundary contours and a raster fill.

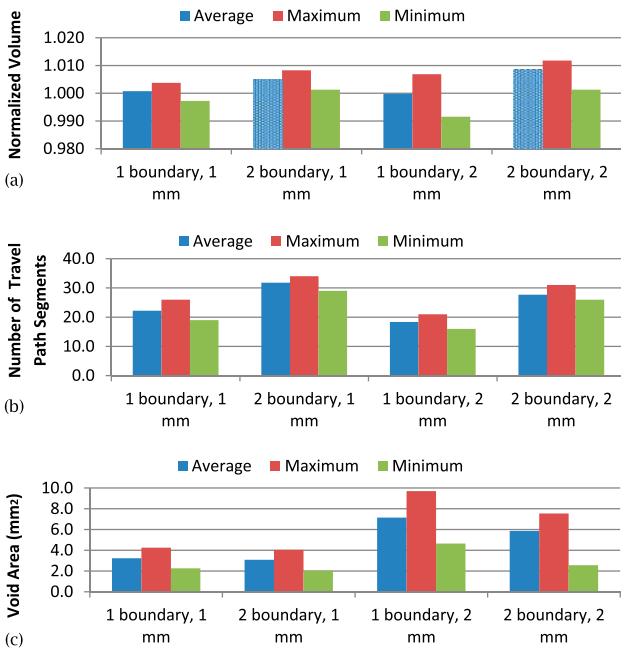


Figure 14. Average, Maximum, and Minimum values for (a) normalized volume, (b) travel path segments, and (c) void area for the four differing process planning build configurations.

bead widths, and 1 and 2 boundary beads. A normalized volume is calculated for comparisons. The voids are along the boundary peripheries (Fig. 12 (a)). The void regions for the 0° raster fill tool path are shown in Fig. 12(b), and a 3D dynamic model created by R is shown in Fig. 12(c).

The normalized travel path for the boundary / bead width options is displayed in Fig. 13. The one boundary - 1 mm width bead @ the fill angle = 0° is the baseline. Here, the two bead boundary solution had the longest travel path - bead area combination for many raster fill angles. However, there is little variability as the bead size is small compared to the bead fill regions' geometry.

Graphs illustrating the means, minimum and maximum values of the normalized deposition volume (travel length x area ellipse), number of bead segments, and the void area are illustrated in Fig. 14. This is a summary for all raster angles. There is slightly more material deposited with the two boundary bead configuration (patterned Average columns). The two boundary bead configuration has more discontinuities (Fig. 14 (b)), and the two mm bead width has larger voids (Fig. 14(c)).

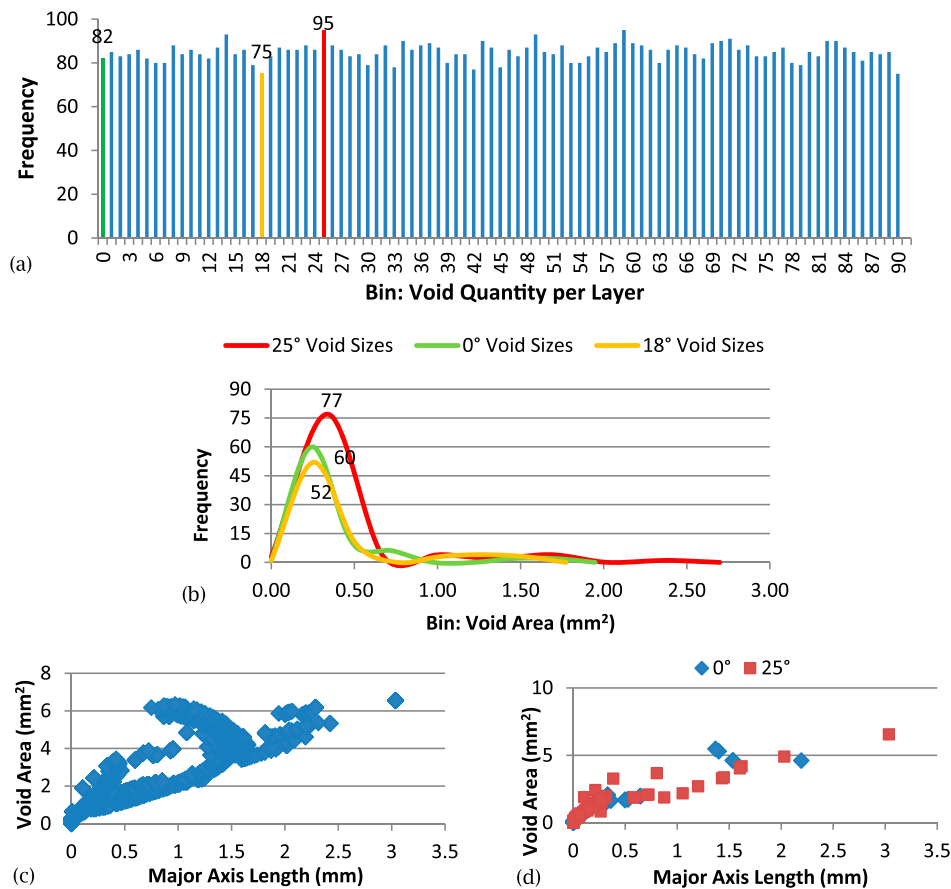


Figure 15. (a) Number of voids per raster fill angle, (b) a frequency plot of the void sizes for three raster fill angles, (c) the void area versus major axis length for all void layers, and (d) the void area versus major axis length for selected void layers.

The void characteristics are plotted for the one boundary bead – 1 mm bead width. The size and quantity are evaluated as well, the void area and ‘major’ axis characteristics. The number of voids per layer varies between 75 and 95 (Fig. 15(a)). The void size that occurs most frequently occurs between 0.25–0.34 mm² for the three ‘typical’ raster angles (Fig. 15(b)). There are few larger voids. The voids area does not necessarily correlate to the major axis length. There is a general trend that can be seen (Fig. 15(c) and (d)), but the voids are not necessary symmetrical, which is indicated by the pattern displayed in Fig. 15(c). Further research needs to be performed to determine whether the major axis length is a desirable parameter to capture.

3.4. Celtic cross

The Celtic cross, similar to the 15 lobed gear, has a bead size that is small compared to the regions to be filled (approx.. 8-10 beads in the narrowest regions); hence, there is little variation with the total travel length (Fig. 16(a) and Tab. 3), but the void shape data is interesting. It can be seen that there are void slivers along the periphery. This introduces a long major axis, although the overall void area may be small (Fig. 16(b)). To explore the void characteristics, the raster angle is rotated in 10° increments, and the void map plotted for one layer, and all layers (Fig. 16(c)).

Although the total voids area is small for each layer, for this part with several curvilinear boundaries, there are

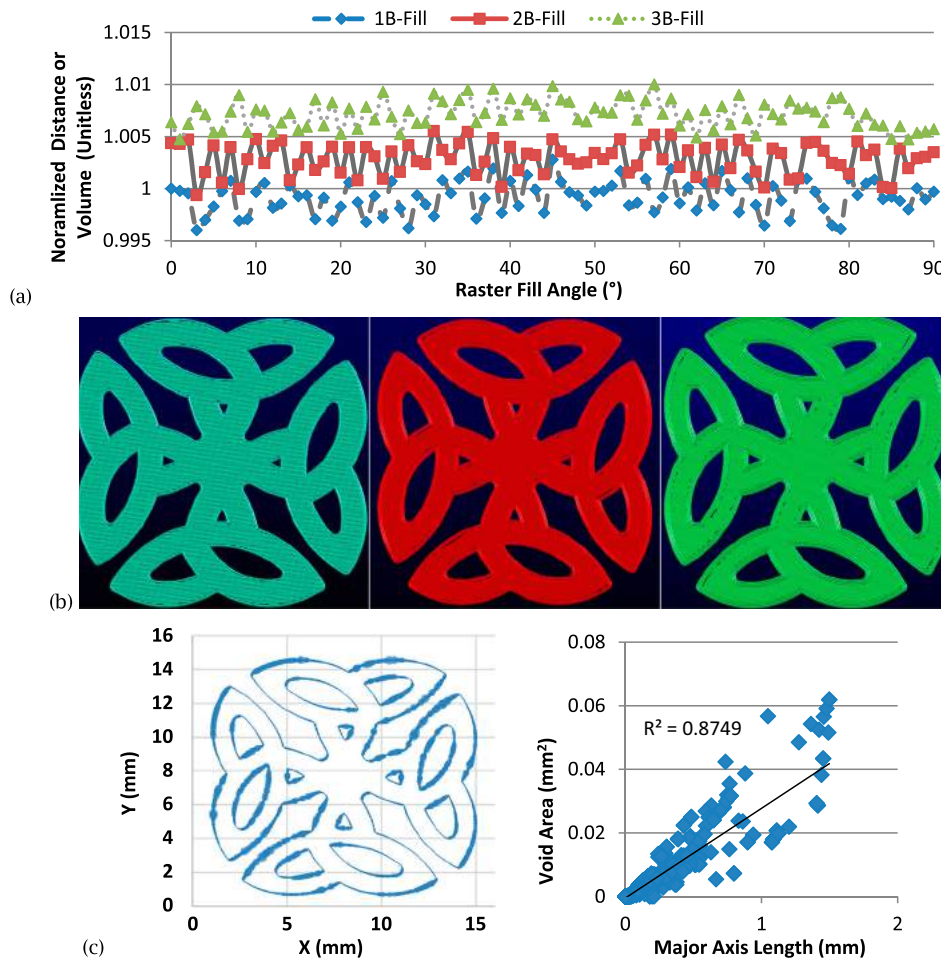


Figure 16. (a) Celtic cross with various boundary and raster fill angle configurations, (b) 3D model for one layer for selected raster angles (0°, 30°, 75°), (c) void map showing void locations & length versus area.

Table 2. Travel path data per raster fill angle summary for n-gon shapes.

Shape	Max. Length	Min. Length	Max. Segments	Min. Segments
4 sides	34°, 56°	3°, 87°	10 @ 28°, 30°, 60°, 62°	1 @ 0-2°, 31-59°, 88-90°
7 sides	57°, 71°	90°, 39°, 38°	5 @ 4°, 22-25°, 29°, 48°, 54°, 55°, 73-77°, 80°, 81°	1 @ 13°, 64°
11 sides	0°, 49°	11°, 38°, 60°	4 @ 33 various fill angles	2 @ 29 various fill angles

Table 3. Macro summary data per selected raster fill angles.

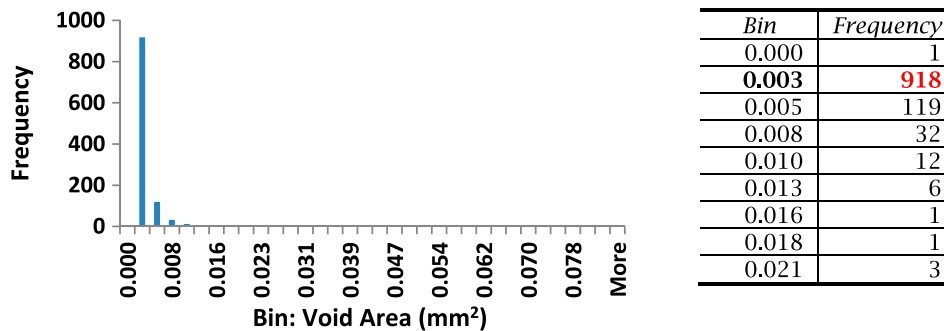
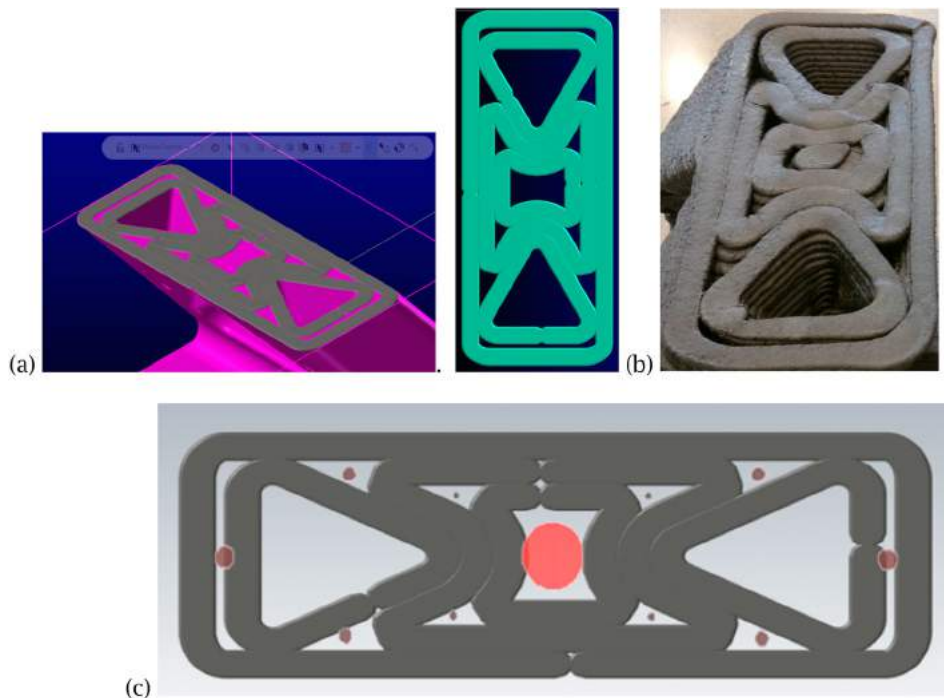
Raster Fill Angle (°)	Toolpath length (mm)	Number of beads	Void Area (sq. mm)
0	1400.2	29	1.80
10	1395.1	36	1.76
20	1401.7	38	1.77
30	1401.4	42	1.75
40	1396.9	45	1.80
50	1402.4	49	1.69
60	1401.7	45	1.71
70	1399.2	35	1.78
80	1396.9	31	1.74
90	1400.3	29	1.79

over 1100 voids per layer. Most of the voids are very small (Fig. 17) and are conceptually similar to pin hole porosity in castings. Approx. 1.25% of the voids have a major axis ≥ 0.5 mm, and 0.33% of the voids have a major axis

length > 1.0 mm. There is a trend between the area and the major axis length for the Celtic cross. The correlation coefficient $R^2 = 0.88$.

3.5. Large bead material extrusion case study

A single layer for a tool path model (Fig. 18(a)), the final built component, and the void analyses are shown for a large bead (0.8 in or 20.3 mm) extrusion process. The material extrusion based AM tool path characteristics lead to predictable outcomes. From this example, the issues with internal sharp corners, filling, and bead to bead and boundary start/stop overlap conditions are illustrated. The tool path model does not show a 'fill' operation in the centre region – this was implemented after a void detection threshold was identified (large

**Figure 17.** Void frequency and sizes for raster fill angle = 0° for the Celtic cross model.**Figure 18.** (a) CAD model and top layer AM tool path, (b) built component, (c) voids analysis with geometry and the R visualization combined – the red circle area is calculated to be.

centre circle), and a void fill routine activated. For the process used in this example, there is a roller to compress the material after it is deposited; hence, the visualization of the bead start-stop conditions does not match the physical component. There are also some ragged edges for the beads, as well as intermittent waves or bulges in the built part (Fig. 18(b)). An overlay of the void area analyses complete with the tool path geometry is shown in Fig. 18(c). The large centre circle is theoretically $3.23 \text{ in}^2 / 2083 \text{ mm}^2$, and the measured area is $3.36 \text{ in}^2 / 2169 \text{ mm}^2$.

4. Discussion

Porosity characterization is standard when implementing casting solutions for a product. However, there is no equivalent for AM material extrusion processes, although voids are inherent with the process. Understanding and managing the voids is necessary to produce functional components. The voids are directly related to the bead size, tool path and the part geometry, and are predictable.

When visualizing the voids for the selected extrusions, it is evident that the voids occur along the periphery geometry and sharp internal corners. The voids are not uniform in size or density, and are influenced by the process parameter settings. This is also true for the number of bead segments and the overall travel length. Changing the process settings will influence the outcomes. When the bead geometry is small compared to the component

being built, there are less voids, and the voids are small and scattered. They are similar to pinhole porosity in castings. Thousands of voids can occur even with a small bead width when there are many curvilinear boundaries. Once the void data is collected, filters can be applied to extract critical void sizes and their locations, and statistical tools can be utilized to extract information with respect to the void characteristics for the complete part or each layer.

R is used to develop algorithms to create 3D graphics to illustrate the void positions and sizes. A dynamic model can be created, and shared. This allows for ready dissemination of essential information. As 3D *.STL files are built for the complete part (Fig. 19), or for selected layers (<https://www.screencast.com/t/daLsKbd76>), this information can be imported into downstream engineering tools for strength or vibration analyses. This information complements the 3D representation in R.

Data management is an issue, as the complex shapes, such as the 15 lobe gear and the Celtric cross, have thousands of voids for the build conditions employed here. The 91 layers to illustrate each raster fill angle ($0^\circ - 90^\circ$) is an artificial build condition, but large components will consist of 100's of layers. Consequently, future research needs to be performed to streamline this analysis prior to establishing optimization strategies. The water pump model is not a 2D extrusion, and the processing time to create the data files is extensive.

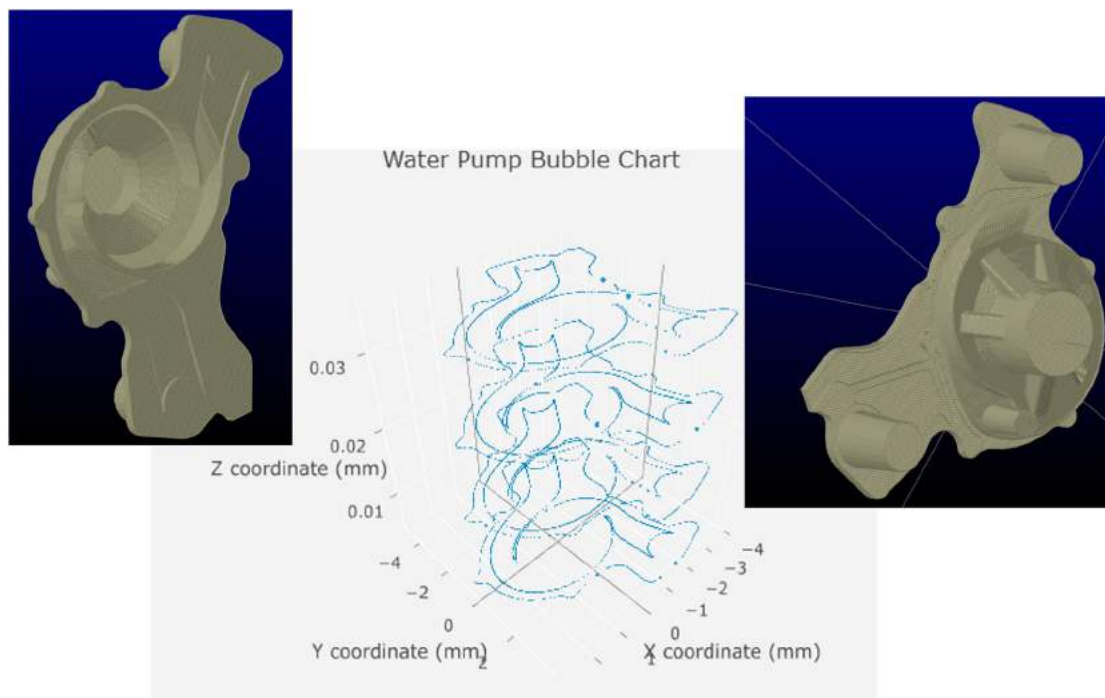


Figure 19. Water Pump STL file, and R bubble chart for 4 build layers showing the voids.

5. Summary, conclusions, and future work

AM tool paths introduce unique quality issues related to voids and discontinuities, and presently there are no tool path quality assessment tools readily available to compare process planning solutions. A multi-perspective set of visualization tools are being developed so that process designers can visualize the void distribution, void area, the total travel path length, and the number of bead segments. This will provide some insight with respect to potential issues. Components will have different functional requirements (i.e. solid with no leak paths or specific damping requirements) that will influence the void reduction or distribution solution. Unlike dealing with castings however, the potential void issues can be known prior to fabrication, and addressed in the process planning stages. However, this research needs to continue to automatically determine optimal build conditions for general shapes, not just basic extrusions. Statistical and visualization tools need to be developed to virtually determine leak paths or chimneys, or to predict problematic regions. Void locations are represented, but not the shapes. Consequently, the major axis and a representative vector or shape metric needs to be evaluated to determine the void shape characteristics. This is ongoing work. Complementary research needs to be performed related to crack propagation and so forth, and quality metrics need to be defined to objectively compare solution approaches to the desired mechanical functional requirements.

Acknowledgements

This research is partially funded by the NSERC Discovery Grant program.

ORCID

R. Jill Urbanic  <http://orcid.org/0000-0002-2906-7618>

Chris G. Burford  <http://orcid.org/0000-0001-8965-8914>

Robert W. Hedrick  <http://orcid.org/0000-0003-2708-6943>

References

- [1] Abele, E.; Stoffregen, H.; Kniepkamp, M.; Lang, S.; Hampe, M.: Selective laser melting for manufacturing of thin-walled porous elements, *Journal of Materials Processing Technology*, 215(1), 2015, 114–122, <https://doi.org/10.1016/j.jmatprot.2014.07.017>.
- [2] Ang, K.C.; Leong, K.F.; Chua, C.K.; Chandrasekaran, M.: Investigation of mechanical properties and porosity relationships in FDM fabricated porous structures, *Rapid Prototyping Journal*, 12(2), 2006, 100–105, <https://doi.org/10.1108/13552540610652447>.
- [3] Asadi-Eydivand, M.; Solati-Hashjin, M.; Farzad, A.; Azuan Abu Osman, N: Effect of technical parameters on porous structure and strength of 3D printed calcium sulfate prototypes, *Robotics and Computer-Integrated Manufacturing*, 37, 2016, 57–67, <https://doi.org/10.1016/j.rcim.2015.06.005>.
- [4] BAAM CI, Big Area Additive Manufacturing, url: <http://www.e-ci.com/baam/>
- [5] Castilho, M.; Gouveia, B.; Pires, I.; Rodrigues, J.; Pereira, M.: The role of shell/core saturation level on the accuracy and mechanical characteristics of porous calcium phosphate models produced by 3Dprinting, *Rapid Prototyping Journal*, 21(1), 2015, 43–55, <https://doi.org/10.1108/RPJ-02/T1/textendash2013-0015>.
- [6] Domingos, M.; Chiellini, F.; Cometa, S.; de Giglio, E.; Grillo-Fernandes, E.; Bartolo, P.; Chiellini, E.: Evaluation of in vitro degradation of PCL scaffolds fabricated via BioExtrusion - Part 2: Influence of pore size and geometry, *Virtual and Physical Prototyping*, 6(3), 2011, 157–165, <https://doi.org/10.1080/17452759.2011.605839>
- [7] Garg, A.; Lam, J.S.L., Savalani, M.M. : A new computational intelligence approach in formulation of functional relationship of open porosity of the additive manufacturing process, *Journal of Advanced Manufacturing Technology*, 80(1–4), 2015, 555–65, <https://doi.org/10.1007/s00170-015-6989-2>.
- [8] Gong, H.; Rafi, K.; Karthik, N.V.; Starr, T.; Stucker, B.: Defect morphology in Ti-6Al-4V parts fabricated by Selective Laser Melting and Electron Beam Melting, 24th International SFF Symposium - An Additive Manufacturing Conference, SFF 2013, 2013, 440–453.
- [9] Gurralla, P.K.; Regalla, S.P.: Part strength evolution with bonding between filaments in fused deposition modelling, *Virtual and Physical Prototyping*, 9(3), 2014, 141–9, <https://doi.org/10.1080/17452759.2014.913400>
- [10] Hedrick, R.; Urbanic, R. J.: Integration of Additive Manufacturing and Virtual Verification Strategies within a Commercial CAM System, *Computer-Aided Design and Applications*, 2012, 10/4: 567–583, <https://doi.org/10.3722/cadaps.2013.567-583>
- [11] LSAM, Large Scale Additive Manufacturing, url: http://www.thermwood.com/lsam_development_main.htm
- [12] MAAM CI, Medium Area Additive Manufacturing, url: <http://www.e-ci.com/maam/>
- [13] Panwisawas, C.; Sovani, Y.; Anderson, M.J.; Turner, R.; Palumbo, N.M.; Saunders, B.C.; Choquet, I.; Brooks, J.W.; Basoalto, H.C.: A multi-scale multi-physics approach to modelling of additive manufacturing in nickel-based superalloys, *Proceedings of the International Symposium on Superalloys*, 2016, 1021–1030, <https://doi.org/10.1002/9781119075646.ch108>.
- [14] Rodriguez, J.F.; Thomas, J.P.; Renaud, J.E.: Design of fused-deposition ABS components for stiffness and strength, *Journal of Mechanical Design*, 2003, 545–551, <https://doi.org/10.1115/1.1582499>.
- [15] R, The R Project for Statistical Computing, url: <https://www.r-project.org/>
- [16] Stratasys FDM Technology, url: <http://www.stratasys.com/3d-printers/technologies/fdm-technology>
- [17] Urbanic, R.J.; DiCecco, L.: Development of Adaptable Light Weighting Methods for Material Extrusion Processes, *ASME IMECE Proceedings*, 2015, <https://doi.org/10.1115/imece2015-51174>